Simultaneous observations of a sporadic E layer by Digisonde and SuperDARN HF radars at Zhongshan, Antarctica

Xiangcai Chen[1], Jianjun Liu[1], Michael J. Kosch[2, 3, 4], Zejun Hu[1], Zhiwei Wang[1, 5], Beichen Zhang[1], Huigen Yang[1], and Hongqiao Hu[1]

1. MNR Key Laboratory for Polar Science, Polar Research Institute of China, Shanghai, China
2. Department of Physics, Lancaster University, Lancaster, United Kingdom
3. South African National Space Agency (SANSA), Hermanus, South Africa
4. Department of Chemistry and Physics, University of KwaZulu-Natal, Westville, South Africa
5. Institute of Space Weather, Nanjing University of Information Science and Technology, Nanjing, China

*Corresponding author: Xiangcai Chen (chenxiangcai@pric.org.cn) and Jianjun Liu (liujianjun@pric.org.cn)

Key points:

1. An Es layer formed in the lower F region and descended to the E region, observed simultaneously by Digisonde and SuperDARN HF radars.
2. The formation and evolution of the Es layer related to the afternoon convection reversal.
3. SuperDARN HF radar measurements suggest the Es layer is elongated with convection circulation.

ABSTRACT

Sporadic E (Es) layers could be composed of metallic ions and formed, modified, or transported by the action of convective electric fields in the high latitude ionosphere. In this paper, by utilizing simultaneous observations from Digisonde and Super Dual Auroral Radar Network (SuperDARN) HF radars at Zhongshan Station (ZHS, 69.4°S, 76.4°E), Antarctica, a thin Es layer, which initially formed in the lower F region and descended into the lower E region, with wavelike structures, was recorded by Digisonde on 14 November 2019. The Es layer-related concurrent ionospheric irregularities were also detected by the SuperDARN ZHS HF radar. By using a global-scale 2-D convection map, combined with images from the Special Sensor Ultraviolet Spectrographic Imager instruments onboard Defense Meteorological Satellite Program (DMSP) spacecraft, it is proposed that the flow shears associated with the duskside convective circulation are responsible for the evolution of the Es layer. Moreover, using the HF radar elevation angle data to measure the scatter height, it is strongly suggested that the Es layerwas elongated with convection circulation. The electrodynamic processes responsible for the formation and evolution of the Es layer are discussed.

1. Introduction

A sporadic E layer, denoted as Es layer, is a sudden ionization enhancement in the ionospheric E region. It usually appears as a narrow band in the height ranges of 90–130 km in the mesosphere and lower thermosphere region. Unlike the molecular ions NO^+ and O_2^+ that are formed by the photoionization of N_2 and O_2, which have lifetimes on the order of seconds, ionization of incoming meteoroid atmospheric ablation, such as Fe^+, Mg^+, and Na^+, produces an Es layer composed of metallic ions that can last several hours and even days (e.g., Plane, 2003). With the suddenly enhanced ionospheric electron density, the Es layer reflects radio waves much more efficiently at higher frequencies and with less absorption. This is sometimes used for high-frequency (HF) radio amateur communications and is also valuable for diagnosing the dynamics, electrodynamics, and ion-chemical processes in the mesosphere and lower thermosphere region (e.g., Bourdillon et al., 1995; Chen et al., 2021; Chisham & Pinnock, 2001).

Observations and simulation results have shown that the mechanism responsible for Es layer formation at mid-latitudes is wind shear (c.f. Haldoupis, 2011, and references therein), while the combined effects of electric fields and neutral winds (Kirkwood & Nilsson, 2000), as well as the abundance of metallic ions (e.g., Bedey & Watkins, 1997), are more important for the formation of Es layers at high latitudes. The convection electric field in polar regions thus provides an important electromagnetic force for convergence/divergence of ion drift (Bristow & Watkins, 1991; Kirkwood & von Zahn, 1991, 1993; Kirkwood & Nilsson, 2000; Nygrén et al., 1984).

According to the convective electric field theory (Kirkwood & Nilsson, 2000), ignoring neutral wind effects, the vertical motion of ions can be expressed as: $v_{iz} = \frac{1}{B_0(1+\rho_i^2)}[E_E + (-)\rho_i E_N] \cos I$, where v_{iz} is the vertical motion of the ions, and ρ_i is the ratio of ion-neutral collision frequency to ion gyrofrequency. E_E and E_N represent the eastward and northward components of the electric field, respectively. I is the magnetic dip angle of the local geomagnetic field B_0. The sign in parentheses refers to the southern hemisphere. With an assumed dawn-dusk electric field at Cambridge Bay (77° CGM lat.), an obvious ion convergence located around 120 km in the pre-midnight hours was observed by MacDougall & Jayachandran (2005) (see their Figure 3c). The Es appeared to form when the convective reversal passed over the observation site. A two-step mechanism responsible for the formation of the Es layer at this 'cusp station' was thus proposed by them. In brief, the Es-related horizontal ionization was firstly concentrated by the convection reversal electric field; then vertical convergence of this enhanced ionization concentration into a moderately narrow Es layers at ~120 km height was achieved by the polar cap dawn-dusk electric field. By investigating the roles of electric field and neutral wind in the generation of Es layers within the polar cap, Nygrén et al. (2008) found that the relative intensity of the electric field comparing to the neutral wind would influence the height of the Es layer and also its density variations. Furthermore, gravity waves may also play an important role in the formation and motion of the Es layer in the vertical direction (e.g., MacDougall et al., 2000a, 2000b).

It is expected that the Es layer could drift horizontally and vertically, but observations of its evolution process are still rare due to the limited field of view of each instrument. Until now, only a few case studies considered the dynamic process of the Es layer in the horizontal and vertical dimensions simultaneously (e.g., MacDougall et al., 2000a). It is therefore still important to extend observations with instruments to further understand the Es layer features at high latitudes. The motivation for this paper is thus to investigate the formation and evolution process of an Es layer at the Zhongshan station (ZHS, -74.9° CGM lat.), Antarctica, and to investigate its morphological characteristics observed by different instruments, as well as to consider its dynamic process in relation to the convective electric field. An overview of the instruments used in this paper is given in section 2. The Es layer observed by the Digisonde and SuperDARN ZHS radars on 14 November 2019 is described in section 3. The formation process of the Es layer and its related ionization enhancement effects on SuperDARN oblique rays are discussed in section 4. A summary of the results is finally given in section 5.

2. Instruments and data sets

2.1. Digisonde radar (DPS-4D)

An ionosonde is a powerful tool that is extensively being used for monitoring real-time ionospheric conditions all over the world. The Digisonde Portable Sounder (DPS-4D) located at ZHS (69.4°S, 76.4°E, LT ≈ UT + 5 h, and MLT ≈ UT + 2 h) was developed by the University of Massachusetts Lowell Center for Atmospheric Research (UMLCAR), and has been in operation since 2010. By utilizing one crossed delta antenna for transmission, and four crossed magnetic dipole antennas for reception, the DPS-4D can adopt the multi-beam sounding mode to get six digitally synthesized off-vertical reception beams, as well as one vertical beam that separates O-mode and X-mode echoes (Reinisch et al., 2009). With 0.05 MHz frequency step sweeping from 0.5 MHz to 9.5 MHz, the amplitude of ionospheric echoes at the height where the local cutoff frequency equals the transmitted frequency were recorded in the ionograms. Finally, using SAO software to manually scale the ionograms with a time interval of 7.5 mins and a height resolution of 2.5 km, the main ionospheric parameters such as Es critical frequency (f_0Es) and its virtual height (h'Es) can be obtained.

2.2. SuperDARN HF radar

The ZHS HF radar, as part of the Super Dual Auroral Radar Network (SuperDARN) in the southern hemisphere, consists of a main array of 16 transmitting/receiving antennas (main array) and a passive array (interferometer) of 4 antennas only for receiving. To obtain sufficient backscatter returns at ionospheric altitudes (i.e. transmitted radio waves refracted and orthogonal to the local magnetic field), SuperDARN radars operate at a variable frequency within 8–20 MHz (Greenwald et al., 1985). By transmitting a multi-pulse sequence with a dwell time of 3 or 7 s on each beam, the backscattered signals are sampled/processed to produce multi-lag complex autocorrelation functions (ACF) as a function of range within 1 or 2 mins (Chisham et al., 2007; Greenwald et al., 1995). Finally, the Doppler line-of-sight velocities can be obtained from a least-square fit to the phase of the complex value of the ACF as a function of lag, while the power and spectral width of the backscatter can be estimated from a Lorentzian or Gaussian fit to the decorrelation of the ACF (Hanuise et al., 1993). Moreover, by measuring the phase delay of backscatter signals between the main array and the passive array, the elevation angle (i.e. the vertical arrival angle) for each range gate can be determined using known information about the radar configuration (e.g., Milan et al., 1997).

Currently, the SuperDARN ZHS radar operates at a frequency of ~10 MHz and scans 16 beams with a dwell time of 3 s for each beam, giving a fan-shaped field-of-view (~54° in azimuth) scanning every 1 min. For each beam, with a pulse length of 300 μs corresponding to a range gate length of 45 km, a total of 75 range gates are sampled. The time lag to the first gate is set at 1200 μs, which means that the radar observes theoretically from 180 to 3555 km range (Hu et al., 2013; Liu et al., 2013). Figure 1 illustrates the relative configuration of the DPS and SuperDARN radars at ZHS for remote sensing. The oblique rays of SuperDARN radar backscatter are primarily from plasma density irregularities in ionospheric E and F regions (ionospheric scatter) (e.g., Chen et al., 2015; Milan & Lester, 2001), reflected from meteor trails in the lower E region (meteor scatter) (e.g., Chisham & Freeman, 2013; Hall et al., 1997), and from the Earth’s surface after reflection/refraction from the ionosphere (ground scatter) (e.g., Huang et al., 2018), but only ionospheric scatter is valuable for our current study. We, therefore, attempt to filter out ground backscatter by removing data with line-of-sight velocities of less than 30 m/s and spectral widths of less than 35 m/s, as well as spectral power lower than 3 dB (Chisham & Pinnock, 2002).

Although the SuperDARN line-of-sight velocities are widely used, more important are the global-scale 2-D plasma convection maps (Chisham et al., 2007; Ruohoniemi & Baker, 1998). By applying the so-called Potential Fit analysis (Ruohoniemi & Baker, 1998), the line-of-sight velocities measured by multiple radars are combined into a common data set for each scan. Hence, the vectors of global plasma convection flow can also be inferred. Specifically, the plasma convection flow measurements are firstly median filtered by several neighboring beams and for three consecutive scans. The smoothed velocities are then sorted to fill a uniform grid of magnetic latitude and longitude equivalent to 1° of magnetic latitude. By fitting the observed grid velocities into a statistical model of plasma flow parameterized by the solar wind and IMF conditions and the Earth's magnetic dipole orientation (e.g., Cousins & Shepherd, 2010), a global-scale 2-D plasma convection map is obtained. As the ionospheric plasma convection is predominantly driven by the electric field in the high latitude regions, its related vectors of electric field and electrostatic potential can also be estimated.

The SuperDARN backscatter elevation angle data has recently been utilized for ionospheric diagnostics. Using the elevation angle of ground scatter echoes, André et al. (1998) derived the critical frequencies in the high-latitude E-region. Milan & Lester (2001) applied it to estimate the altitude of ionospheric backscatter. For the classical SuperDARN virtual height model with mapping errors (e.g., Chen et al., 2015, 2016, 2017; Yeoman, et al., 2001, 2008), Chisham et al. (2008) proposed an improved range-finding algorithm based on a statistical analysis of backscatter elevation angle of arrival information. Moreover, Gillies et al. (2009, 2010, 2011) applied the elevation angle for estimating the refractive index of the ionospheric plasma to improve the SuperDARN velocity measurements. After that, the estimated refractive index is further utilized to monitor the F-region maximum electron densities (Ponomarenko et al., 2011). The above mentioned methods for determining the ground range and refractive index of ionospheric scattering volumes were systematically evaluated by Greenwald et al. (2017). Due to the intrinsic technical difficulties with direct calibration of a time offset between the two antenna arrays (Ponomarenko et al., 2015, 2018), getting reliable measurements of echo elevation angles is painstaking. Nevertheless, the relatively straightforward algorithm (e.g., Milan et al., 1997) gives reasonably accurate results, which has recently been evaluated systematically by Shepherd (2017).

In this study, both SuperDARN ZHS beam data and convection map in the Southern Hemisphere are used. A snapshot of the global plasma convection map at 16:00 – 16:02 UT is shown on the right panel of Figure 1. The collocated DPS-4D and SuperDARN ZHS radars thus form an especially good geometry for investigating the ionospheric plasma dynamic process.

2.3. Defense Meteorological Satellite Program (DMSP)/SSUSI

With a far-ultraviolet (FUV) imager, i.e. the Special Sensor Ultraviolet Spectrographic Imager (SSUSI), onboard the Defense Meteorological Satellite Program (DMSP) spacecraft, the FUV emissions in 5 bands can be recorded by cross-track scanning (Paxton et al., 2002). A series of DMSP satellites operating at an altitude of ~840 km, with an inclination of ~98.9° and a period of ~101 minutes, are sun-synchronous, polar-orbiting around the Earth (Hardy et al., 1984). Each scanning image is built up over 20–30 minutes when the satellite flies over the polar region. During this study, the DMSP F17 and F18 were sequentially (spacing of ~4–5 mins) crossing the Southern Hemisphere. Hence, we only employ the SSUSI LBHS (140–160 nm) emission from DMSP F17, which is primarily produced by precipitating electrons and secondary electrons produced by precipitating protons.

3. Observational results

3.1. Es layer observed by DPS

Figure 2 shows a sequence of 7.5 min interval ionograms for ~15:37 – 17:30 UT on 14 November 2019. A thin Es layer initially formed at ~260 km (virtual height) and suddenly occurs in the field-of-view of Digisonde shown in Figure 2c. This thin Es layer became stratified at a time after 16:22 UT (see Figure 2g), with sometimes discontinuous features in the frequency range (see Figure 2i), echoes spread in height (see Figures 2k and 2l), and a secondary echo such as shown in Figure 2o. The Es layer finally descents from the lower F region into the lower E region.

To examine the altitude and temporal evolution of the Es layer in detail, Figure 3 presents the height-time-amplitude of the echoes (i.e. integration of the echo amplitude) recorded by the DPS-4D at sounding frequency ranges of 3.5–3.75 MHz (3a), 6.5–6.75 MHz (3b), and greater than 2 MHz (3c) during the time interval of 13:00–21:00 UT. From Figures 3a and 3c, the ionospheric echoes from the F region are mainly above the virtual height of 250 km. is the F-region was almost completely obscured by the Es layer for time intervals of ~18:15–18:45, and ~19:45–20:15 UT. The critical frequency (peak height) of the F2 layer gradually decreased (uplift) from ~4 (~200) to 2.5 MHz (220 km) during this time interval, which is associated with the diminished photoionization due to sunset. The Es layer suddenly occurred at the lower F region and subsequently descended into the E region (<140 km) with an average speed of ~43.5 (±7.35) m/s as estimated from Figure 3b. This morphology, called intermediate layer (indicated by arrows in Figure 3b), has been extensively reported and simulated by many studies at mid-latitudes (e.g., Bishop & Earle, 2003; Mathews et al., 2001), and is expected to be modulated by horizontal wind field and tidal winds. Here, we still address this intermediate layer as an Es layer because of its continuous evolution. Subsequently, the Es layer shows ascend/descend wavelike features for about ~3.5 h, and finally disappeared out of the field-of-view of the DPS-4D at ~20:15:10 UT. As shown in Figure 3b, the lowest virtual height of the Es layer is separately observed at 17:30:10, 18:30:10, 19:30:10 UT, which appears to be a periodic perturbation of about 1 h. It seems like that the period of the descending Es layer corresponded to strong ionization enhancements (i.e. large integration of the echo amplitude shown in Figure 3c). Nevertheless, the f_0Es can not be properly estimated at time intervals of ~16:00–16:15, ~16:52–17:15, and ~18:00–18:45 UT, due to the upper limit of the DPS sounding frequency at 9.5 MHz.

3.2. Es layer observed by SuperDARN ZHS radar

The Es layer-related ionospheric echoes are also detected by the collocated SuperDARN ZHS radar. A range gate versus time plot of Doppler line-of-sight velocities for beams 13(a), 7(b), and 1(c) from 13:00 to 21:00 UT is shown in Figure 4. Three intervals with differential backscatter features can be easily identified. Before ~15:10 UT, seen in Figures 4a and 4b, the HF radar echoes are mainly backscattered from range gates greater than 5 (i.e. slant ranges from 405 to 990 km), which is expected to be ionospheric echoes with 1/2-hop from the F region. Subsequently, the HF radar ionospheric returns are also detected in the near-range gates. These ionospheric echoes show periodic-like flow, which is delineated by the black lines in Figure 4c. The third interval of ionospheric echoes is mainly observed in the far ranges (i.e. range gate> 9) at a time after ~18:00 UT, which is also expected to be the 1/2-hop backscatter from the ionospheric F region.

Although all three panels in Figure 4 display similar ionospheric characteristics, some differences exist, such as the ionospheric echoes were rarely observed in beam 1 before 15:30 UT. This means that the HF radar beams remotely sound different ionosphere regions. To further understand the ionospheric conditions for Es layer formation, four ionospheric plasma convection maps from the SuperDARN network overlaid with the SSUSI LBHS images from DMSP F17 crossing are depicted in Figure 5. To ease the comparison of these two data sets, two color codes have been applied to represent plasma flow (color from reddish black to yellow) and auroral activities (color from green to yellowish-white), respectively. The time for each convection map corresponds, approximately, to the satellite position somewhere in the middle of each plot. Similar to Figure 1b, the field-of-view of the ZHS radar is illustrated by the dashed blue line, and the red star indicates the location of ZHS. In addition, the thick red curve represents the Heppner–Maynard Boundary, which in general represents the equatorward boundary of the auroral oval (e.g., Imber et al., 2013; Wang et al., 2022).

In the early phase of the Es occurrence shown in Figure 5a, three regions of plasma flow within the field-of-view of ZHS radar are observed. Just poleward of the auroral oval around 78° MLAT, the plasma flow with convection reversal is spatially localized between 18 and 21 MLT. This is associated with the ionospheric flow shear observed by beam 13 around 15:36 UT in Figure 4a. An eastward convection flow roughly located at the auroral oval around 21–23 MLT is observed. This is also identified by HF radar beam 1 at range gates of 10–15 at this time in Figure 4c. The observational evidence strongly demonstrates that the ZHS is located under the auroral oval before the appearance of the Es layer. This conclusion could also be verified by the ionospheric echoes from virtual heights of ~140–190 km shown in Figure 3c before 16:30 UT, which signifies the possible particle precipitation with an energy of ~ keV. Nevertheless, the poleward boundary of the auroral oval is observed by HF radar beams 13 and 7.

For the next two satellite crossings shown in Figures 5b and 5c, two spatially localized plasma flows are observed. The large-scale eastward convection flows around midnight are situated at far ranges in the polar cap, while plasma flownear the auroral oval poleward boundary (and/or auroral arc) was observed with low velocities at near ranges. The sheared plasma flow over ZHS associated with aurora emissions may be expected (e.g., Liu et al., 2011), and was observed by the HF radar line-of-sight velocities (indicated by arrows in Figure 3). Finally, for the end phase shown in Figure 5d, ZHS was located in the polar cap region, even though the HMB represents the auroral oval boundary incorrectly. The Es layer had disappeared from the field of view of the DPS. Joint satellite and ground radar observations confirm that the spatial-temporal formation and evolution of the Es layer were associated with the afternoon convection reversal.

Line-of-sight plasma drift velocities towards the radar were continuously observed in the near range gates (see Figure 4), which implies that the plasma was convected from the F region to the E region (see the sketch map in Figure 1). To further clarify the Es layer-related ionization enhancement detected by DPS-4D that is also monitored by the SuperDARN ZHS radar, Figure 6a shows the occurrence distribution of elevation angles from different beams for range gates 0–18, i.e. green, blue, and black histograms for beams 13, 7 and 1, during this time interval. Assuming spherical propagation geometry and straight-line propagation, the virtual height of the ionospheric scatter volume from radar beams can be estimated as

$$h = \sqrt{R_E^2 + r^2 + 2R_E r sin\alpha} - R_E$$

where R_E is the Earth's radius, the slant range (r) is determined by the center of the effective scatter volume at 180 km + 45/2 km + gate×45 km, and α is the elevation angle for the corresponding range gate. Figures 6b–6d show the scatterplot of backscatter altitude versus time with slant ranges for three radar beams. The lowest virtual height of the Es layer and its associated stratified/sublayers observed by the DPS-4D are also overlaid as red histogram and asterisk, respectively. Additionally, the peak height of the F2 layer (i.e. hmF2), scaled from ionograms, is plotted as black dots in Figure 6c. Although the straight-line propagation assumption may not be true, the hmF2 denoted in Figure 6c can be treated as a demarcation altitude with backscatter from the F region above and from the Es-related E region below. The ionospheric echoes in the E region (i.e. < 150 km) from beams 13 and 7 precede the appearance of Es observed by DPS. The ionospheric echoes from beam 1 are closely associated with the evolution of the Es layer and its related sublayers (red asterisk) from 260 to 150 km. As the majority values of elevation angle from beams 13 and 1 are higher than from beam 7, as shown in Figure 6a, some ambiguity is present near the lowest altitude of Es layer. One reason is due to ignoring the effects of refraction, which tends to produce an overestimation of the true altitude of the scatter volume by about 10–20 km (Milan & Lester, 2001). Another reason may be the classic algorithm for acquiring elevation angle values at ZHS without considering a nonzero X component (see Shepherd, 2017 for more details). Nonetheless, these ambiguities can not cause a serious impact on our height comparison.

4. Discussion

4.1. Dynamic process of Es layer

We have observed a thin Es layer initially formed in the lower F region followed by a descent into the E region, which is especially different from the normal Es layer usually formed in the E region about 90–130 km. With the duration of the Es layer observed by DPS-4D of more than 3 hours, an abundance of metallic ions within the Es layer is expected (MacDougall et al., 2000a), which could be transported by the approximately equatorward directed convective electric field (Bedey & Watkins, 1997; Nygren et al., 1984; Parkinson et al., 1998). The plasma flow in the polar ionosphere is modulated by the large-scale convection electric field. A simple model presented by Bedey & Watkins (1997) has shown that metallic ions could be lifted from the nominal background metallic layer below 100 km into the lower F region on the dayside. With the flow horizontally through the polar cap and toward the nightside, Bedey & Watkins (1997) proposed that the metallic ions could form in a narrow vertical stream (~50 km) and precipitate within a limited band of geomagnetic latitudes (see their Figure 6). Their results clearly showed that the abundance of the metallic ions enhanced only in a small portion of the region where westerly electric field dominated (in the northern hemisphere) and ion precipitation predominantly occurred before local midnight. For our current study of the long-lived thin Es layer at ZHS, Antarctica, we are concerned with the ionospheric E-F region coupling effect caused by the Es layer. A southward electric field associated with eastern plasma flow (see Figure 4) dominates the evolution process of the Es layer from the lower F region to the E region, which means that an anti-sunward plasma drift is occurring over the site. Nevertheless, an ion motion gradient that exists in the F region should be a precondition for the initial convergence of the Es layer.

As mentioned in the Introduction, MacDougall & Jayachandran (2005) suggested that a two-step formation mechanism is responsible for the Es formation at a 'cusp latitude' station, i.e. firstly horizontal convergence of ionization by the afternoon convection reversal electric field, and then vertical convergence of this ionization by the mainly dawn-dusk electric field in the polar cap. By carefully checking the DMSP/SSUSI data (see Figure 5), we recognize that the ZHS station was shifted from the duskside auroral oval into the polar cap. The initial formation of the Es layer in the lower F region observed by the DPS at ~15:50 UT would correspond to the poleward boundary of the auroral oval. Moreover, the last convection reversal is also clearly observed by the SuperDARN radar beam 13 at time ~20:15 UT (see Figure 4a). This implies that the initial formation of the Es layer at the lower F region would be due to the duskside convection reversal passing over the ZHS. It also suggests that once the ionospheric convection reversal condition is suitable for the metallic ions to converge, the Es layer would be formed even in the lower F region.

The Es layer descended with an average vertical speed of ~43.5 m/s, i.e. estimated from the time interval of ~15:52–16:37 UT and from 260 to 142.5 km. Considering the convection electric fields within the descending period, we estimate the electric field contributes to the vertical velocity about 15 m/s on average, which means the action of gravity waves and/or tidal waves must be responsible for the descending of the Es layer. The stratified features of the Es layer shown in Figure 2 and wave-like ionospheric echoes that were both detected by the DPS (see Figure 3) and SuperDARN radar (see Figure 4c) are strong evidence for the action of gravity waves. Similar features were also observed and explained by MacDougall et al. (2000a). With the Es layer descent into the E region, a combined electric field and neutral wind, as well as a gravity wave (e,g, Kirkwood & Nilsson, 2000) resulting in the observed wave-like motion of the Es layer, are expected. This Es layer contained metallic sodium ions with wave-like motions in the lower E region resulting in the neutralization of sodium atoms that produced a sporadic sodium layer that has recently been reported by Chen et al. (2021).

4.2. SuperDARN backscatter returns refracted by Es layer

The Es layer-related ionization enhancement is accompanied by simultaneous coherent backscatter echoes from the F region at far ranges to the E region in the near ranges in SuperDARN ZHS radar. These ionospheric features strongly indicate the existence of electrical coupling between the E and F regions along the geomagnetic field. Observations of ionospheric irregularities associated with the Es layer were also reported by Ogawa et al. (2009) in the Japanese sector. The SuperDARN ZHS radar monitors the Es layer from the F to E regions as shown in Figure 6, indicating that there is a continuous supply of decameter-scale irregularities associated with the enhanced ionospheric electron density.

To quantitatively estimate the Es layer-related electron density that results in the bending of ray paths from the ZHS HF radar, we use Ponomarenko et al.'s (2011) technique to evaluate the maximum electron density in the far range F region and near range E region, respectively. Assuming the ionosphere is spherically stratified and symmetric so that Snell's law applies for the rays launched at an elevation angle (α, at the radar site) and reaching the orthogonality condition in the ionosphere at the height of hs, the refractive index of the ionospheric plasma can be written as (Gillies et al., 2009):

$$n_r = \frac{R_E}{R_E + h_s}\frac{cos\,\alpha}{sin\,I}$$

where R_E is the Earth's radius (i.e. 6370 km), I represents the geomagnetic inclination at the backscatter points, and h_s is the scatter echo height. Since the refraction index of HF radio waves at frequency f_0 is related to the plasma frequency f_p as

$$f_p = f_0\sqrt{1 - n_r^2}$$

the maximum electron density at the Es layer can be evaluated from

$$N_m Es = \frac{4\pi^2 m\varepsilon_0 f_p^2}{e^2}$$

where m and e are the electron mass and charge and ε_0 is the permittivity of free space.

We use the elevation angle data from beam 7, which is closest to a uniform distribution of angle values (see Shepherd, 2017 Figure 4d). For the initial formation of the Es layer in the lower F region, *hs* was ~260 km, and the onset elevation angle value was ~39.95°, which corresponds to a refractive index n_r of about ~0.76. The derived maximum electron density (i.e. NmEs) by the ZHS radar is ~0.55×10^6 cm^{-3}, which is only half of the Digisonde measurement of ~1.12×10^6 electrons/cm^3. For the final Es echoes recorded by the SuperDARN ZHS radar in the near range gates around 20:00 UT, the elevation angle of ~20° corresponds to a refractive index of 0.97. The peak electron density of 0.76×10^5 cm^3 derived by the SuperDARN radar is ~3.8 times smaller than the Digisonde measurement of ~2.9×10^5 electrons/cm^3.

Assessing the quality of the peak electron density estimates made from elevation angle measurements by the SuperDARN Rankin Inlet (RKN) radar was recently carried out by Koustov et al. (2020). By comparing the SuperDARN RKN results to ionosonde and incoherent scatter radar measurements, the underestimation of peak electron density by SuperDARN radar (by up to 30% in their cases) could be mainly due to low background electron densities (Koustov et al., 2020). However, there are other effects that also very likely contribute to our current measurements. One is the Digisonde that detects signals from localized regions with the strongest electron density, while the SuperDARN ZHS radar range gate, with a spatial resolution of 45 km, could smooth out the peak electron densities. This smoothing effect is expected to be stronger for ionospheric conditions with higher patchiness and poorer propagation conditions (Koustov et al., 2020). Secondly, the critical frequency is manually acquired from Digisonde ionograms containing the extraordinary wave, which has a higher frequency than the ordinary wave, i.e. O-mode wave, by half the electron gyrofrequency. Last but not least, the Digisonde and SuperDARN ZHS radar detected the Es layer from different locations. However, the measurement results will not influence our conclusion that the SuperDARN ZHS radar oblique rays experience significant ionospheric refraction, resulting in bending of radio paths, by the Es layer.

4.3. The elongation of the Es layer

The Es layer initially forms in the lower F region and descends into the E region, which is detected by both the DPS-4 Digisonde and SuperDARN ZHS radar. As seen from Figure 6c, the onset time of the ionospheric echoes monitored by the SuperDARN ZHS radar at 200 km precedes the DPS detections by about 60 min. The time of the Es layer detected by the DPS at 200 km corresponds to the disappearance of the Es-related ionospheric irregularities at the same height (i.e. ~16:30 UT). As the SuperDARN ZHS radar scans in azimuth to the west of the site, it is expected that the Es layer formed in the lower F region, as detected by the HF radar, will be transported by the convective circulation. The range from the center of the effective scatter volume of the SuperDARN range gate 7 to the field-of-view of the DPS corresponds to about 483 (±57.7) km at 200 km altitude in the F region. Assuming the Es layer-related plasma flow is always equal to the large-scale convection velocity, i.e. ~174 m/s on average, the Es layer will take ~46 (±5.5) min to travel 483 km. This means that it is possible the Es layer was formed as an enhanced ionization patch with a size of about 500 km and then transported with the ionospheric convection circulation.

Bedey & Watkins (1997) have suggested that the Es layer related metallic ions can be lifted from the background ion layer into the F region, where the ions can then be transported over large distances before "precipitating" in relatively narrow bands in latitude (see their Figure 6). Furthermore, they expected that the Es layer related ions are deposited in the lower E region within a very narrow band of latitudes, 74°–76° and 76°–77° MLAT for westerly field strengths of 50 mV/m and 10 mV/m, respectively. During this time interval, the electric field was on average less than ~12 mV/m (see Chen et al., 2021, Figure 1c), the Es layer initially formed at a latitude of ~78° MLAT in the lower F region and descended to around 75° MLAT in the lower E region as observed by the SuperDARN radar (see Figure 5). Bedey & Watkins's (1997) model analysis yields results that are in good agreement with our current observations, which strongly demonstrates that the formation of the Es layer is due to the large-scale redistribution of metallic ions via horizontal transport in the F region (e.g., MacDougall & Jayachandran, 2005) followed by a descent into the lower E region within a narrow band (Bedey & Watkins, 1997).

5. Summary

In this paper, we have studied the dynamic process of an Es layer simultaneously observed by the DPS Digisonde and SuperDARN ZHS radars at Zhongshan, Antarctica. As the ionospheric Es layer has a significant impact on radio wave propagation, the traditional techniques that only employ a single instrument, such as ionosonde for Es layer observation, are not sufficient to resolve the morphology and dynamics of the Es layer in the spatial domain. We show a unique example of an Es layer, which initially formed in the lower F region and then descended into the lower E region. This is expected to result from a two-step formation mechanism involving horizontal convergence of ionization by the electric fields of the duskside convection reversal, and then vertical convergence of this enhanced ionization by the electric fields (MacDougall & Jayachandran, 2005). The initial formation of the Es layer-related convection reversal was detected by the SuperDARN line-of-sight velocity, while its subsequent evolution process was related to the auroral activity at the poleward boundary of the auroral oval, which is confirmed by images of SSUSI LHBS emission from the DMSP spacecraft. The Es-related ionization enhancement also gives rise to SuperDARN radar refraction bending the beam into the lower F and E regions. The occurrence of the Es layer has a time lag between the DPS and SuperDARN radar observations, which can be simply explained by the large-scale convection circulation at the lower F region. This implies that the Es layer is elongated as an enhanced ionization patch with a size of about 500 km. Utilizing a multi-instrument to study the evolution processes of the Es layer thus has significant implications for understanding electrodynamics and electrical coupling between the E and F regions in the polar region.

Data Availability Statement

The ZHS DPS and SuperDARN data can be download from the Data Centre for Meridian Space Weather

Monitoring Project webpage (http://data.meridianproject.ac.cn), while the SuperDARN 2-D convection map and the electric field is available from the Virginia Tech portal (http://vt.superdarn.org). The DMSP/SSUSI LBHS data is available from Data Products | SSUSI (jhuapl.edu) (https://ssusi.jhuapl.edu/data_products)

Acknowledgments

This work was supported by the National Key Research and Development Program of China (Grant NO. 2021YFE0106400 and 2018YFC1407300), the National Natural Science Foundation of China (Grant NO. 42130210, 42120104003, 41704159, and 41831072), and the fund from the Institute of Applied Meteorology. H. G. Yang was supported by Shanghai Science and Technology Innovation Action Plan (No. 21DZ1206100). The author also acknowledges the use of ZHS DPS and HF radar data from the Chinese Meridian Project. SuperDARN is a collection of scientific HF radars funded by the national science funding agencies of Australia, Canada, China, France, Italy, Japan, Norway, South Africa, the United Kingdom, and the United States of America. Thanks to the Johns Hopkins University Applied Physics Laboratory for providing the DMSP/SSUSI auroral FUV data.

References

André, D., G. J. Sofko, K. Baker, and J. MacDougall (1998), SuperDARN interferometry: Meteor echoes and electron densities from ground scatter, *Journal of Geophysical Research: Space Physics*, *103*(A4), 7003-7015.

Bedey, D. F., and B. J. Watkins (1997), Large-scale transport of metallic ions and the occurrence of thin ion layers in the polar ionosphere, *Journal of Geophysical Research Space Physics*, *102*(A5), 9675-9681, doi:10.1029/96ja03825.

Bishop, R. L., and G. D. Earle (2003), Metallic ion transport associated with midlatitude intermediate layer development, *Journal of Geophysical Research*, 108(A1), doi:10.1029/2002ja009411.

Bourdillon, A., C. Haldoupis, and J. Delloue (1995), High-frequency Doppler radar observations of magnetic aspect sensitive irregularities in the midlatitude E region ionosphere, *Journal of Geophysical Research: Space Physics*, 100(A11), 21503-21521, doi:10.1029/95ja01079.

Bristow, W. A., and B. J. Watkins (1991), Numerical simulation of the formation of thin ionization layers at high latitudes, *Geophysical Research Letters*, *18*(3), 404-407, doi:10.1029/90GL02588.

Chen, X. C., D. S. Han, D. A. Lorentzen, K. Oksavik, J. I. Moen, and L. J. Baddeley (2017), Dynamic Properties of Throat Aurora Revealed by Simultaneous Ground and Satellite Observations, *Journal of Geophysical Research: Space Physics*, *122*, 3469-3486, doi:10.1002/2016JA023033.

Chen, X. C., D. A. Lorentzen, J. I. Moen, K. Oksavik, and L. J. Baddeley (2015), Simultaneous ground-based optical and HF radar observations of the ionospheric footprint of the open/closed field line boundary along the geomagnetic meridian, *Journal of Geophysical Research: Space Physics*, *120*(11), 9859-9874, doi:10.1002/2015JA021481.

Chen, X. C., D. A. Lorentzen, J. I. Moen, K. Oksavik, L. J. Baddeley, and M. Lester (2016), F region ionosphere effects on the mapping accuracy of SuperDARN HF radar echoes, *Radio Science*, *51*(5), 490-506, doi:10.1002/2016rs005957.

Chen, X., Huang, W., Ban, C., Kosch, M. J., Murphy, D. J., Hu, Z., et al. (2021). Dynamic properties of a sporadic sodium layer revealed by observations over Zhongshan, Antarctica: A case study. *Journal of Geophysical Research: Space Physics*, 126, e2021JA029787. https://doi.org/10.1029/2021JA029787.

Chisham, G., et al. (2007), A decade of the Super Dual Auroral Radar Network (SuperDARN): scientific achievements, new techniques and future directions, *Surveys in Geophysics*, *28*(1), 33-109, doi:10.1007/s10712-007-9017-8.

Chisham, G., and M. P. Freeman (2013), A reassessment of SuperDARN meteor echoes from the upper mesosphere and lower thermosphere, *Journal of Atmospheric and Solar-Terrestrial Physics*, 102, 207-221, doi:10.1016/j.jastp.2013.05.018.

Chisham, G., and M. Pinnock (2001), Assessing the contamination of SuperDARN global convection maps by non-F-region backscatter, *Annales Geophysicae*, 20(1), 13-28. https://doi.org/10.5194/angeo-20-13-2002

Chisham, G., T. K. Yeoman, and G. J. Sofko (2008), Mapping ionospheric backscatter measured by the SuperDARN HF radars - Part 1: A new empirical virtual height model, *Annales Geophysicae*, *26*(4), 823-841, doi:10.5194/angeo-26-823-2008.

Cousins, E., and S. Shepherd (2010), A dynamical model of high-latitude convection derived from SuperDARN plasma drift measurements, *Journal of Geophysical Research: Space Physics*, 115(A12), doi:10.1029/2010JA016017.

Gillies, R. G., G. C. Hussey, G. J. Sofko, K. A. McWilliams, R. A. D. Fiori, P. Ponomarenko, and J. P. St.-Maurice (2009), Improvement of SuperDARN velocity measurements by estimating the index of refraction in the scattering region using interferometry, *Journal of Geophysical Research*, *114*(A7), A07305, doi:10.1029/2008ja013967.

Gillies, R. G., G. C. Hussey, G. J. Sofko, P. V. Ponomarenko, and K. A. McWilliams (2011), Improvement of HF coherent radar line-of-sight velocities by estimating the refractive index in the scattering volume using radar frequency shifting, *Journal of Geophysical Research*, *116*(A1), A01302, doi:10.1029/2010ja016043.

Gillies, R. G., G. C. Hussey, G. J. Sofko, D. M. Wright, and J. A. Davies (2010), A comparison of EISCAT and SuperDARN F-region measurements with consideration of the refractive index in the scattering volume, *Journal of Geophysical Research*, *115*(A6), A06319, doi:10.1029/2009ja014694.

Greenwald, R. A., et al. (1995), DARN/SuperDARN A global view of the dynamics of high-latitude convection, *Space Science Reviews*, *71*(1-4), 761-796, doi:10.1007/BF00751350.

Greenwald, R. A., K. B. Baker, R. A. Hutchins, and C. Hanuise (1985), An HF phased-array radar for studying small-scale structure in the high-latitude ionosphere, *Radio Science*, *20*(1), 63-79, doi:10.1029/RS020i001p00063.

Greenwald, R. A., N. Frissell, and S. de Larquier (2017), The importance of elevation angle measurements in HF radar investigations of the ionosphere, *Radio Science*, *52*(3), 305-320, doi:10.1002/2016RS006186.

Haldoupis, C. (2011), A Tutorial Review on Sporadic E Layers, in *Aeronomy of the Earth's Atmosphere and Ionosphere*, edited by M. A. Abdu and D. Pancheva, pp. 381-394, Springer Netherlands, Dordrecht, doi:10.1007/978-94-007-0326-1_29.

Hall, G. E., J. W. MacDougall, D. R. Moorcroft, J.-P. St.-Maurice, A. H. Manson, and C. E. Meek (1997), Super Dual Auroral Radar Network observations of meteor echoes, *Journal of Geophysical Research: Space Physics*, 102(A7), 14603-14614, doi:10.1029/97ja00517.

Hanuise, C., J. Villain, D. Gresillon, B. Cabrit, R. Greenwald, and K. Baker (1993), Interpretation Of HF radar ionospheric Doppler spectra by collective wave scattering-theory, *Annales Geophysicae*, 11, 29-39.

Hardy, D. A., L. K. Schmitt, M. S. Gussenhoven, F. J. Marshall, and H. C. Yeh (1984), Precipitating electron and ion detectors (SSJ/4) for the block 5D/Flights 6-10 DMSP (Defense Meteorological Satellite Program) satellites: Calibration and data presentation *Rep. Air Force Geophysics Laboratory*

Hu, H., E. Liu, R. Liu, H. Yang, and B. Zhang (2013), Statistical characteristics of ionospheric backscatter observed by SuperDARN Zhongshan radar in Antarctica, *Advances in Polar Science*, *24*(1), 19-31, doi:10.3724/SP.J.1085.2013.00019.

Huang, D., E. Liu, H. Hu, and J. Liu (2018), Algorithm for the estimation of ionosphere parameters from ground scatter echoes of SuperDARN, *Science China Technological Sciences*, 61(11), 1755-1764, doi:10.1007/s11431-017-9178-4.

Imber, S. M., S. E. Milan, and M. Lester (2013), The Heppner-Maynard Boundary measured by SuperDARN as a proxy for the latitude of the auroral oval, *Journal of Geophysical Research: Space Physics*, 118(2), 685-697, doi:10.1029/2012ja018222.

Kirkwood, S., and H. Nilsson (2000), High-latitude Sporadic-E and other Thin Layers – the Role of Magnetospheric Electric Fields, *Space Science Reviews*, *91*(3), 579-613, doi:10.1023/A:1005241931650.

Kirkwood, S., and U. von Zahn (1993), Formation Mechanisms for Low-AltitudeEsand Their Relationship with Neutral Fe Layers: Results from the METAL Campaign, *Journal of Geophysical Research*, *98*(A12), 21549-21561, doi:10.1029/93ja02644.

Kirkwood, S., and U. V. Zahn (1991), On the role of auroral electric fields in the formation of low altitude sporadic-E and sudden sodium layers, *Journal of Atmospheric & Terrestrial Physics*, *53*(5), 389-407, doi:10.1016/0021-9169(91)90034-5.

Koustov, A. V., S. Ullrich, P. V. Ponomarenko, R. G. Gillies, D. R. Themens, and N. Nishitani (2020), Comparison of SuperDARN peak electron density estimates based on elevation angle measurements to ionosonde and incoherent scatter radar measurements, *Earth Planets Space*, *72*(1), 43, doi:10.1186/s40623-020-01170-w.

Liu, E. X., H. Q. Hu, K. Hosokawa, R. Y. Liu, Z. S. Wu, and Z. Y. Xing (2013), First observations of polar mesosphere summer echoes by SuperDARN Zhongshan radar, *Journal of Atmospheric and Solar-Terrestrial Physics*, *104*, 39-44, doi:10.1016/j.jastp.2013.07.011.

Liu, J. J., H. Q. Hu, D. S. Han, T. Araki, Z. J. Hu, Q. H. Zhang, H. G. Yang, N. Sato, A. S. Yukimatu, and Y. Ebihara (2011), Decrease of auroral intensity associated with reversal of plasma convection in response to an interplanetary shock as observed over Zhongshan station in Antarctica, *Journal of Geophysical Research: Space Physics*, 116, A03210, doi:10.1029/2010ja016156.

MacDougall, J. W., and P. T. Jayachandran (2005), Sporadic E at cusp latitudes, *Journal of Atmospheric and Solar-Terrestrial Physics*, *67*(15), 1419-1426, doi:10.1016/j.jastp.2005.07.011.

Macdougall, J. W., P. T. Jayachandran, and J. M. C. Plane (2000a), Polar cap Sporadic-E: Part 1, Observations, *Journal of Atmospheric and Solar-Terrestrial Physics*, *62*(13), 1155-1167, doi:10.1016/S1364-6826(00)00093-6.

Macdougall, J. W., J. M. C. Plane, and P. T. Jayachandran (2000b), Polar cap Sporadic-E: part 2, modeling, *Journal of Atmospheric and Solar-Terrestrial Physics*, *62*(13), 1169-1176, doi:10.1016/S1364-6826(00)00092-4.

Mathews, J. D., D. W. Machuga, and Q. Zhou (2001), Evidence for electrodynamic linkages between spread-F, ion rain, the intermediate layer, and sporadic E: results from observations and simulations, *Journal of Atmospheric and Solar-Terrestrial Physics*, 63(14), 1529-1543, doi:https://doi.org/10.1016/S1364-6826(01)00034-7.

Milan, S., T. Jones, T. Robinson, E. Thomas, and T. Yeoman (1997), Interferometric evidence for the observation of ground backscatter originating behind the CUTLASS coherent HF radars, *Annales Geophysicae*, *15*(1), 29-39.

Milan, S. E., and M. Lester (2001), A classification of spectral populations observed in HF radar backscatter from the E region auroral electrojets, *Annales Geophysicae*, *19*(2), 189-204, doi:10.5194/angeo-19-189-2001.

Nygrén, T., L. Jalonen, J. Oksman, and T. Turunen (1984), The role of electric field and neutral wind direction in the formation of sporadic E-layers, *Journal of Atmospheric and Terrestrial Physics*, *46*(4), 373-381, doi:10.1016/0021-9169(84)90122-3.

Nygrén, T., M. Voiculescu, and A. T. Aikio (2008), The role of electric field and neutral wind in the generation of polar cap sporadic E, *Annales Geophysicae*, *26*, 3757-3763, doi:10.5194/angeo-26-3757-2008.

Ogawa, T., N. Nishitani, Y. Otsuka, K. Shiokawa, T. Tsugawa, and K. Hosokawa (2009), Medium-scale traveling ionospheric disturbances observed with the SuperDARN Hokkaido radar, all-sky imager, and GPS network and their relation to concurrent sporadic E irregularities, *Journal of Geophysical Research: Space Physics*, *114*(A3), A03316, doi:10.1029/2008ja013893.

Parkinson, M. L., P. L. Dyson, D. P. Monselesan, and R. J. Morris (1998), On the role of electric field direction in the formation of sporadic E -layers in the southern polar cap ionosphere, *Journal of Atmospheric and Solar-Terrestrial Physics*, *60*(4), 471-491, doi:10.1016/0021-9169(84)90122-3.

Paxton, L. J., D. Morrison, Y. Zhang, H. Kil, B. Wolven, B. S. Ogorzalek, D. C. Humm, and C.-I. Meng (2002), Validation of remote sensing products produced by the Special Sensor Ultraviolet Scanning Imager (SSUSI): a far UV-imaging spectrograph on DMSP F-16, SPIE.

Plane, J. M. C. (2003), Atmospheric chemistry of meteoric metals, *Chemical Reviews*, *103*(12), 4963-4984, doi:10.1021/cr0205309.

Ponomarenko, P., N. Nishitani, A. V. Oinats, T. Tsuya, and J.-P. St.-Maurice (2015), Application of ground scatter returns for calibration of HF interferometry data, *Earth, Planets and Space*, *67*(1), 138, doi:10.1186/s40623-015-0310-3.

Ponomarenko, P., J. P. St.-Maurice, and K. A. McWilliams (2018), Calibrating HF Radar Elevation Angle Measurements Using E Layer Backscatter Echoes, *Radio Science*, *53*(11), 1438-1449, doi:10.1029/2018rs006638.

Ponomarenko, P. V., A. V. Koustov, J. P. St.-Maurice, and J. Wiid (2011), Monitoring the F-region peak electron density using HF backscatter interferometry, *Geophysical Research Letters*, *38*(21), L21102, doi:10.1029/2011gl049675.

Reinisch, B. W., I. A. Galkin, G. M. Khmyrov, A. V. Kozlov, K. Bibl, I. A. Lisysyan, G. P. Cheney, X. Huang, D. F. Kitrosser, and V. V. Paznukhov (2009), New Digisonde for research and monitoring applications, *Radio Science*, *44*(1), 1-15, doi:10.1029/2008RS004115.

Ruohoniemi, J. M., and K. B. Baker (1998), Large-scale imaging of high-latitude convection with Super Dual Auroral Radar Network HF radar observations, *Journal of Geophysical Research*, 103(A9), 20797, doi:10.1029/98ja01288.

Shepherd, S. G. (2017), Elevation angle determination for SuperDARN HF radar layouts, *Radio Science*, *52*(8), 938-950, doi:10.1002/2017rs006348.

Wang, Z., Lu, J., Hu, H., Liu, J., Hu, Z., Wang, M., et al. (2022). HMB Variations Measured by SuperDARN During the Extremely Radial IMFs: Is the coupling function applicable in radial IMF? *Journal of Geophysical Research: Space Physics*, 127, e2021JA029589. https://doi.org/10.1029/2021JA029589

Yeoman, T. K., G. Chisham, L. J. Baddeley, R. S. Dhillon, T. J. T. Karhunen, T. R. Robinson, A. Senior, and D. M. Wright (2008), Mapping ionospheric backscatter measured by the SuperDARN HF radars - Part 2: Assessing SuperDARN virtual height models, *Annales Geophysicae*, *26*(4), 843-852, doi:10.5194/angeo-26-843-2008.

Yeoman, T. K., D. M. Wright, A. J. Stocker, and T. B. Jones (2001), An evaluation of range accuracy in the Super Dual Auroral Radar Network over-the-horizon HF radar systems, Radio Science, 36(4), 801-813, doi:10.1029/2000rs002558.

Figure Captions:

Figure 1: (left) Simulation of ray tracing for the SuperDARN radar at Zhongshan Station. Rays are traced for elevation angles from 5° to 55° and group ranges from 0 to 2400 km for beam 7 and at a frequency of 10 MHz. The electron density profiles are provided by the IRI Model for 14 November 2019 at 18:00 UT (~23:10 LT). The red ray represents the last high-angle that can be refracted back to the ground. While the black lines with a 30° off-zenith angle show the maximum field-of-view of Digisonde. (right) An example of the SuperDARN 2-D convection map plotted at 16:00–16:02 UT in MLAT–MLT coordinates in the southern hemisphere. Noon/dawn is toward the top/right. The ionospheric flow measurements are indicated by a dot with a line attached, the color of which gives the magnitude of flow and the line shows the direction. The + and × symbols are the maximum/minimum of the electrostatic potential distribution, where the positive equipotential contours are shown by black dashed lines and negative contours are solid. The red closed curve shows the Heppner-Maynard Boundary. The field-of-view of the ZHS HF radar is shown by a dashed fan, and directions of beams 13, 7, and 1 are also denoted. The red star represents the ZHS station.

Figure 2: Sequence of 7.5 min interval ionograms for ~15:37 – 17:30 UT on 14 November 2019, which show the initial formation and subsequent evolution of the Es layer.

Figure 3: Height-time-amplitude of the echoes from the DPS at sounding frequency ranges of 3.5–3.75 MHz (a), 6.5–6.75 MHz (b), and larger than 2 MHz (c).

Figure 4: Range versus time plots from the ZHS HF radar ionospheric line-of-sight velocities for beams 13(a), 7(b), and 1(c). Positive (negative) line-of-sight velocities are toward (away from) the radar. The black lines in the bottom panel indicate the Es layer-related ionospheric echoes, while the arrows indicate the shear flow resulting from the auroral arc.

Figure 5: Four plots of SuperDARN 2-D convection maps overlaid with images recorded by the SSUSI instrument in the LBHS wavelength when the DMSP F17 crossing.

Figure 6: (a) Histograms of the elevation angle values from HF radar beams 13 (green), 7 (blue), and 1 (black) at range gates of 0–18, during the time interval of 13:00–21:00 UT. (b–d) Scatterplots of backscatter altitude versus time for three radar beams. The overlaid red histogram and asterisks represent the lowest virtual height of the Es layer and its stratified/sublayers observed by the DPS. The black dots show the peak height of the F2 layer scaled from ionograms.

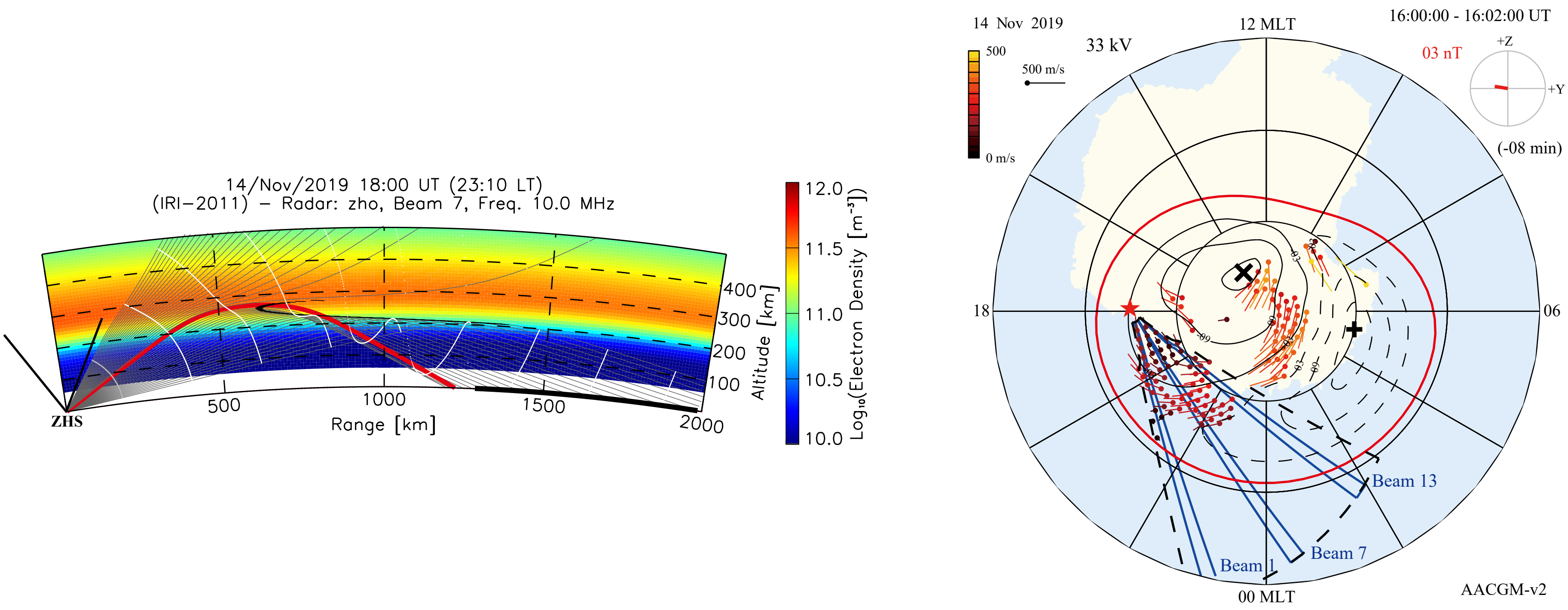
14/Nov/2019 18:00 UT (23:10 LT)
(IRI−2011) − Radar: zho, Beam 7, Freq. 10.0 MHz
ZHS
500
1000
1500
2000
Range [km]
100
200
300
400
Altitude [km]
12.0
11.5
11.0
10.5
10.0
Log₁₀(Electron Density [m⁻³])
14 Nov 2019
500
0 m/s
500 m/s
33 kV
12 MLT
16:00:00 - 16:02:00 UT
03 nT
+Z
+Y
(-08 min)
18
06
Beam 13
Beam 7
Beam 1
00 MLT
AACGM-v2

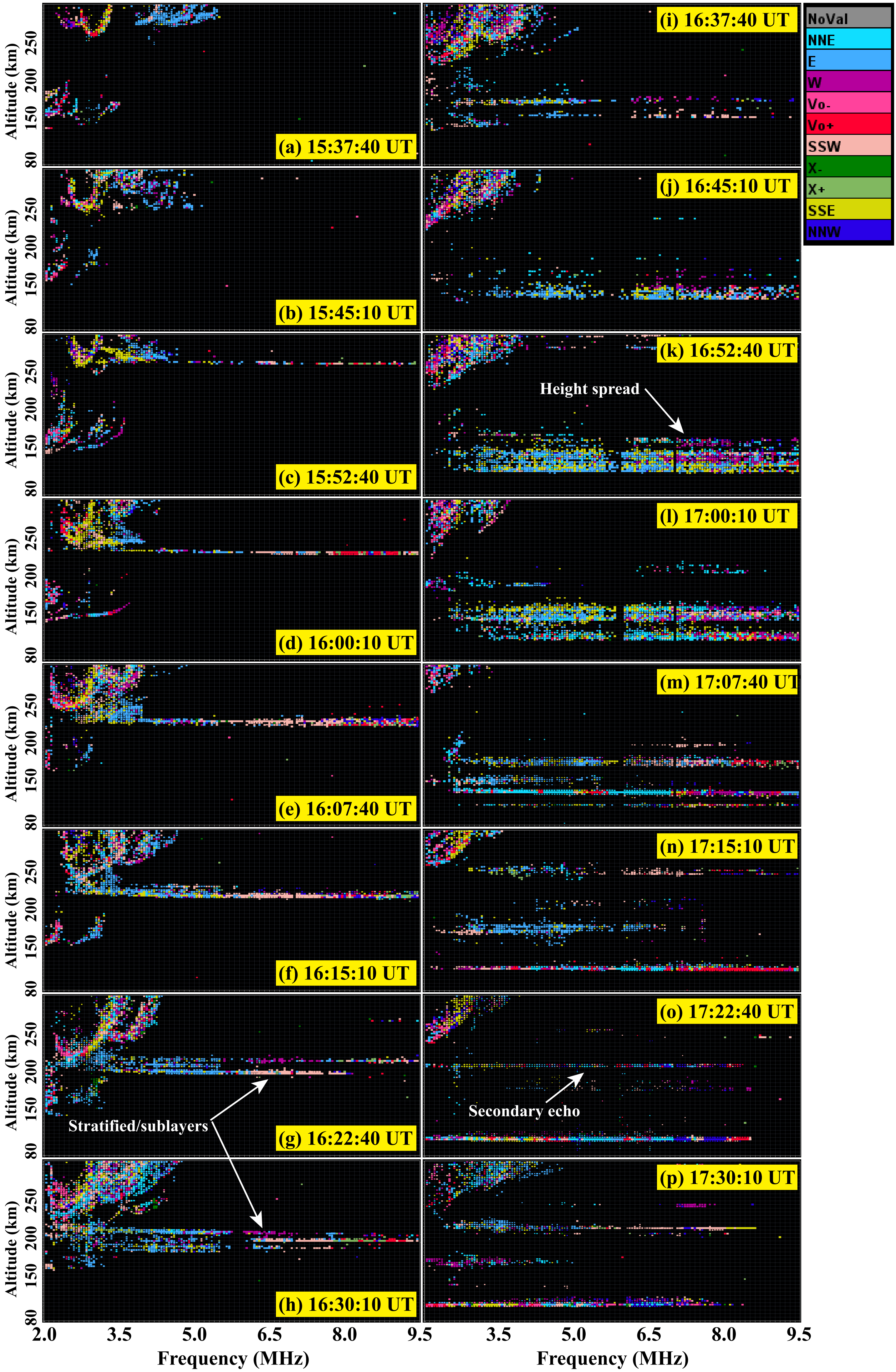

NoVal
NNE
E
W
Vo-
Vo+
SSW
X-
X+
SSE
NNW
(a) 15:37:40 UT
(b) 15:45:10 UT
(c) 15:52:40 UT
(d) 16:00:10 UT
(e) 16:07:40 UT
(f) 16:15:10 UT
(g) 16:22:40 UT
(h) 16:30:10 UT
(i) 16:37:40 UT
(j) 16:45:10 UT
(k) 16:52:40 UT
(l) 17:00:10 UT
(m) 17:07:40 UT
(n) 17:15:10 UT
(o) 17:22:40 UT
(p) 17:30:10 UT
Height spread
Secondary echo
Stratified/sublayers
Altitude (km)
80
150
200
250
Frequency (MHz)
2.0
3.5
5.0
6.5
8.0
9.5

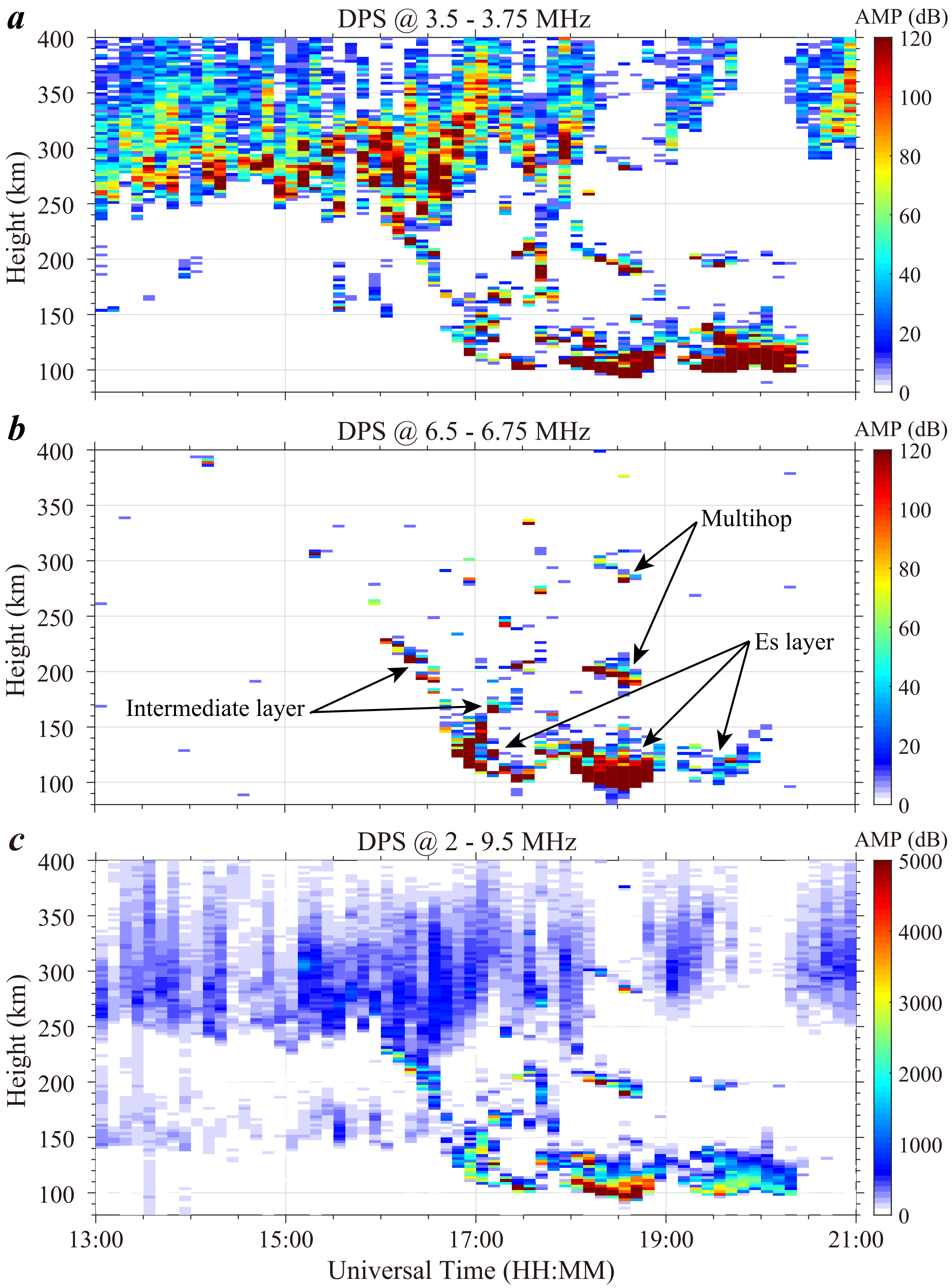
a
DPS @ 3.5 - 3.75 MHz
AMP (dB)
Height (km)
b
DPS @ 6.5 - 6.75 MHz
Multihop
Es layer
Intermediate layer
c
DPS @ 2 - 9.5 MHz
Universal Time (HH:MM)
13:00
15:00
17:00
19:00
21:00

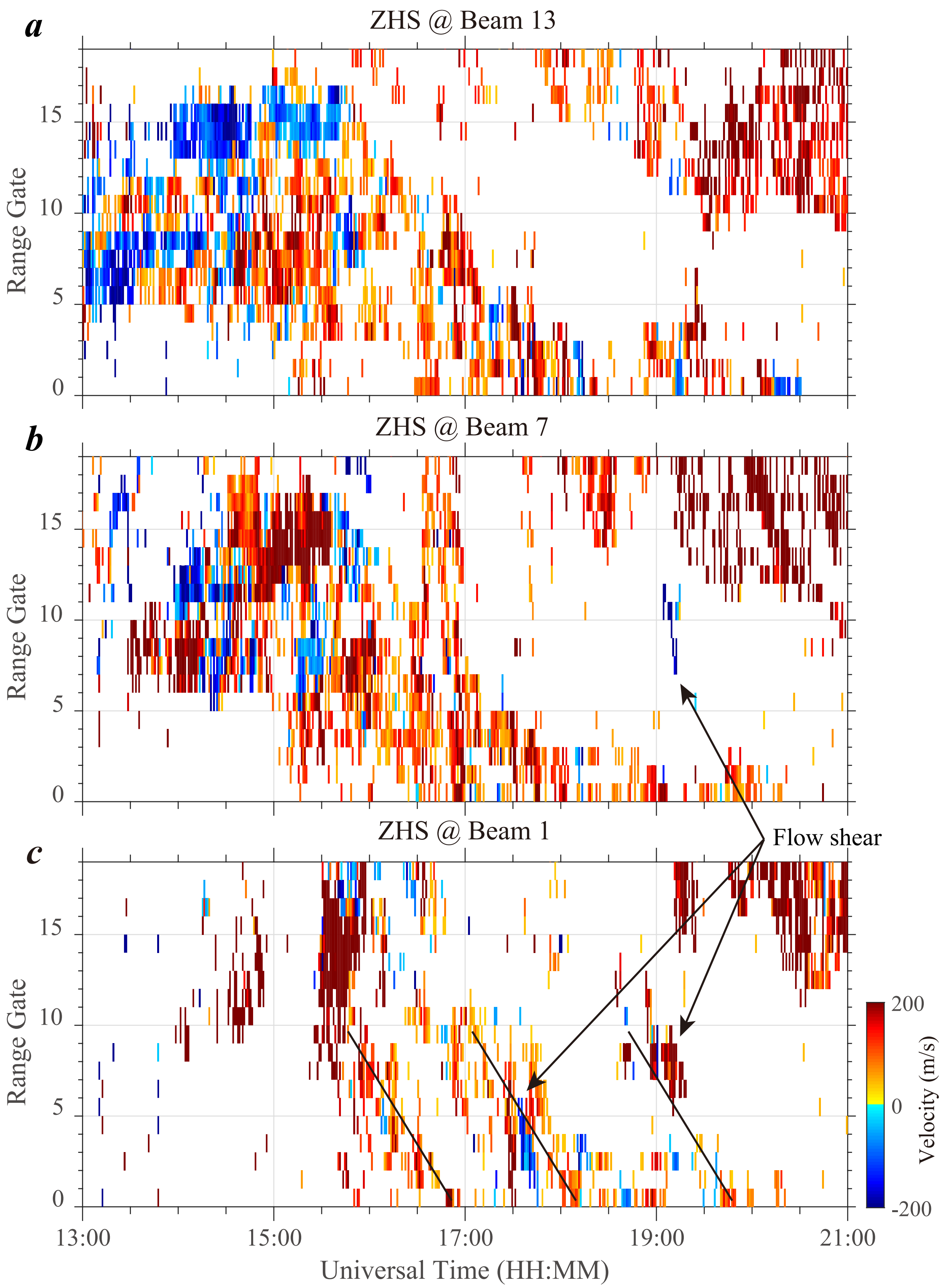
a
ZHS @ Beam 13
b
ZHS @ Beam 7
c
ZHS @ Beam 1
Range Gate
0
5
10
15
Flow shear
13:00
15:00
17:00
19:00
21:00
Universal Time (HH:MM)
Velocity (m/s)
200
0
-200

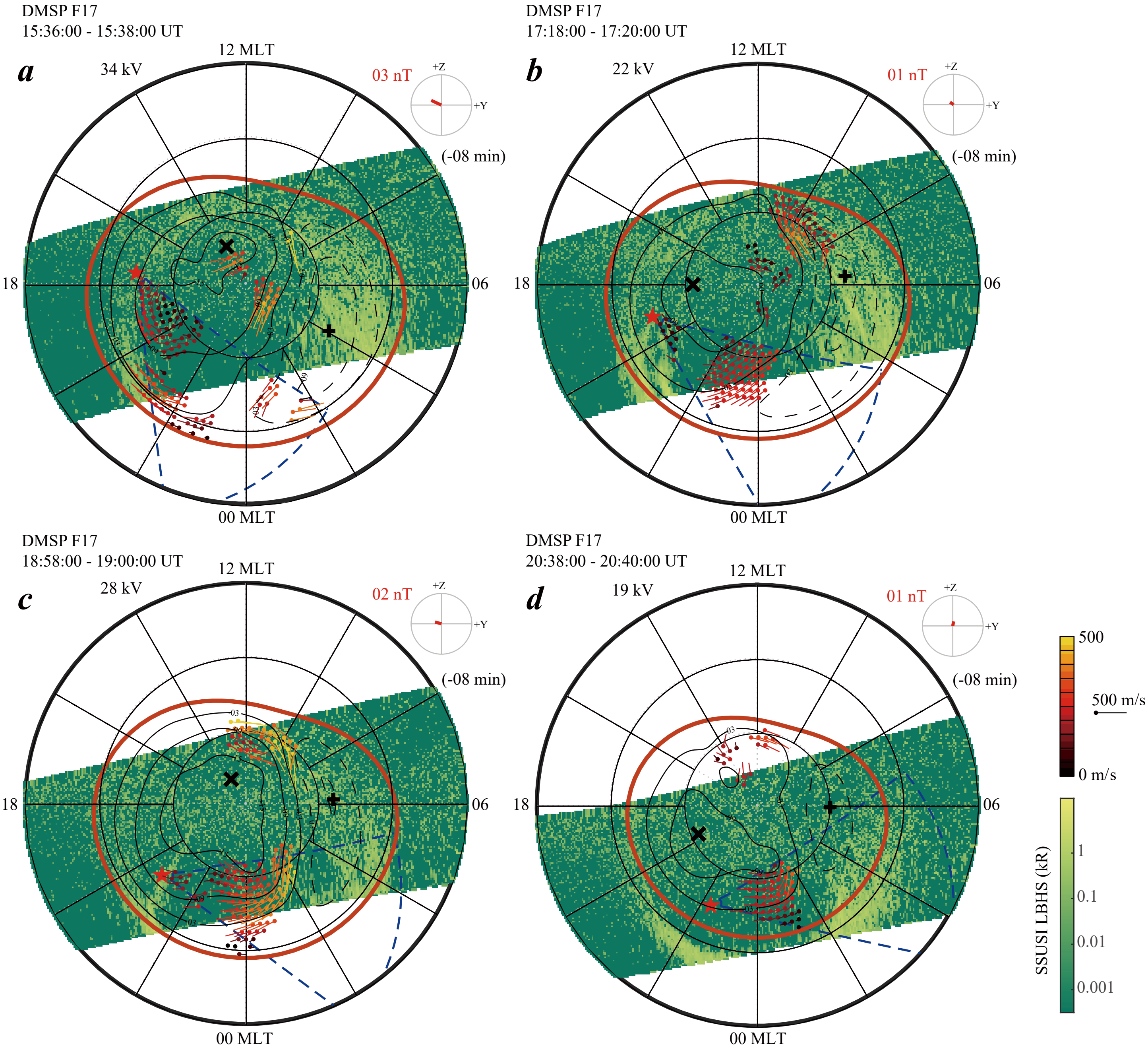

DMSP F17
15:36:00 - 15:38:00 UT
a
12 MLT
34 kV
03 nT
+Z
+Y
(-08 min)
18
06
00 MLT
DMSP F17
17:18:00 - 17:20:00 UT
b
12 MLT
22 kV
01 nT
+Z
+Y
(-08 min)
18
06
00 MLT
DMSP F17
18:58:00 - 19:00:00 UT
c
12 MLT
28 kV
02 nT
+Z
+Y
(-08 min)
18
06
00 MLT
DMSP F17
20:38:00 - 20:40:00 UT
d
12 MLT
19 kV
01 nT
+Z
+Y
(-08 min)
18
06
00 MLT
500
500 m/s
0 m/s
SSUSI LBHS (kR)
1
0.1
0.01
0.001

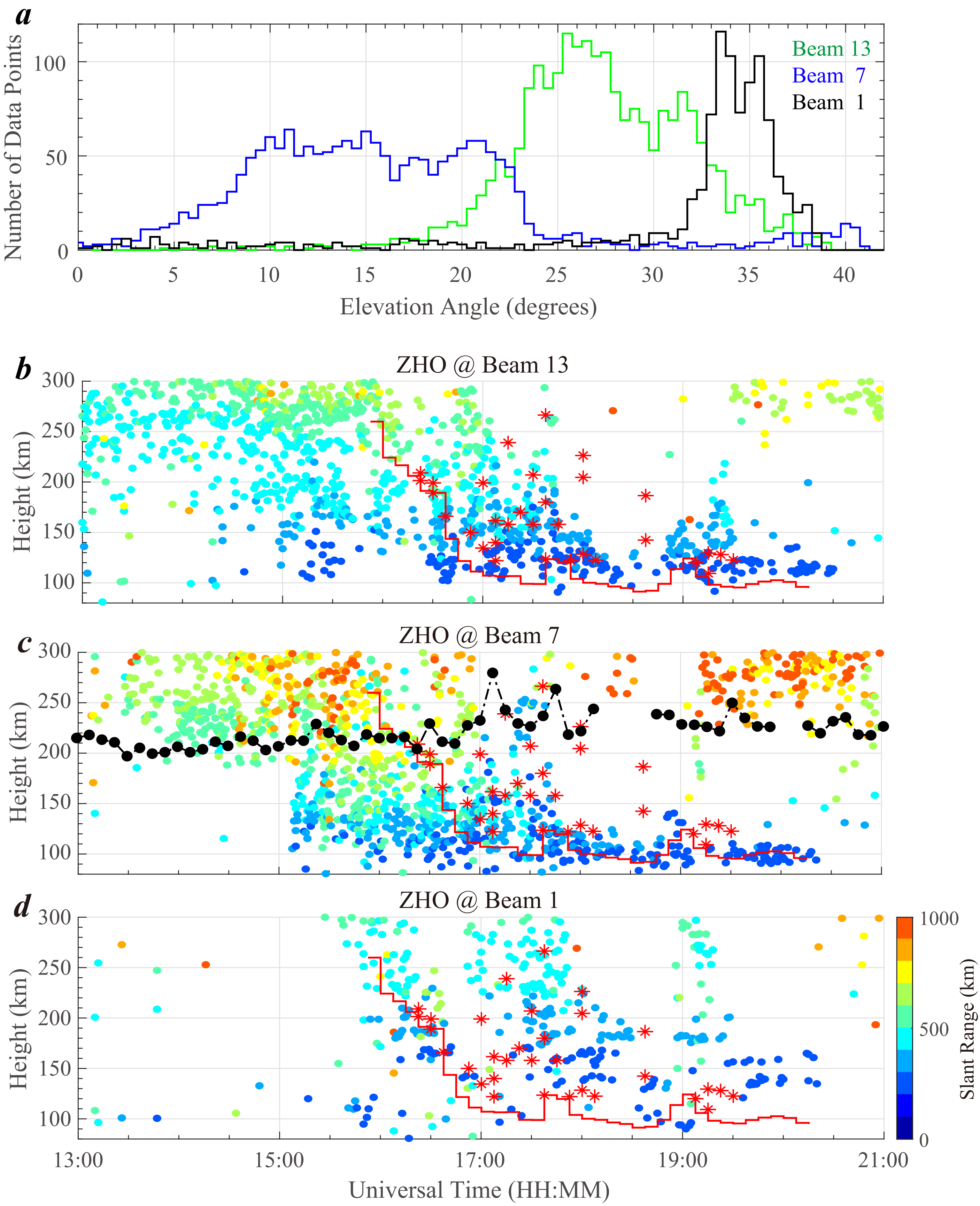
a
Number of Data Points
Elevation Angle (degrees)
Beam 13
Beam 7
Beam 1
b
ZHO @ Beam 13
Height (km)
c
ZHO @ Beam 7
Height (km)
d
ZHO @ Beam 1
Height (km)
Universal Time (HH:MM)
Slant Range (km)
13:00
15:00
17:00
19:00
21:00